jmb Article

The Solution Structure of Rabbit IgG Accounts for Its Interactions with the Fc Receptor and Complement C1q and Its Conformational Stability

Lucy E. Rayner[1], Nilufar Kadkhodayi-Kholghi[1], Richard K. Heenan[2], Jayesh Gor[1], Paul A. Dalby[3] and Stephen J. Perkins[1]

*1 - **Department of Structural and Molecular Biology,** Division of Biosciences, Darwin Building, University College London, Gower Street, London WC1E 6BT, UK*
*2 - **ISIS Facility,** Science and Technology Facilities Council, Rutherford Appleton Laboratory, Harwell Oxford, Didcot OX11 0QX, UK*
*3 - **Department of Biochemical Engineering,** University College London, Torrington Place, London WC1E 7JE, UK*

Correspondence to Stephen J. Perkins: *s.perkins@ucl.ac.uk*
http://dx.doi.org/10.1016/j.jmb.2012.11.019
Edited by R. Huber

Abstract

Solution structures for antibodies are critical to understand function and therapeutic applications. The stability of the solution structure of rabbit IgG in different buffers and temperatures was determined by analytical ultracentrifugation and X-ray and neutron scattering. Rabbit IgG showed a principally monomeric species, which is well resolved from small amounts of a dimeric species. The proportion of dimer increased with increased concentration, decreased temperature and heavy water from 8% to 25% in all buffers except for high salt (250 mM NaCl). The Guinier X-ray radius of gyration R_G likewise increased with concentration in 137 mM NaCl buffer but was unchanged in 250 mM NaCl buffer. The Guinier neutron R_G values increased as the temperature decreased. The X-ray and neutron distance distribution curves $P(r)$ revealed two peaks, *M1* and *M2*, whose positions did not change with concentration to indicate unchanged structures under all these conditions. The maximum dimension increased with concentration because of dimer formation. Constrained scattering modeling reproducibly revealed very similar asymmetric solution structures for monomeric rabbit IgG in different buffers, in which the Fab–Fc and Fab–Fab pairs were separated by maximally extended hinge structures. The dimer was best modeled by two pairs of Fab regions forming tip-to-tip contacts. The intact rabbit IgG structures explained the ability of its two ligands, the Fc receptor and complement C1q, to bind to the top of its Fc region that is fully accessible and unhindered by the Fab regions.
© 2012 Elsevier Ltd. All rights reserved.

Introduction

Antibody function is mediated through antigen binding activities in the Fab regions, including the neutralization of pathogens and agglutination (cross-linking). Antibody effector mechanisms occur through the Fc region and include complement activation through C1q binding and antibody-dependent cell-mediated cytotoxicity through antibody binding to Fc receptors (FcRs) on immune effector cells. Antibody binding to FcRs is important to enable them to identify and destroy antibody-tagged cells in the immune response, and different FcRs are expressed on different immune cells. The human IgG subclasses IgG1, IgG2, IgG3 and IgG4 differ in their abilities to activate complement and bind to FcRs.[1] In application to industry, these differences mean that antibody therapeutics are predominantly based on the most abundant IgG1 subclass or on IgG4, which does not activate complement. They include rituximab (lymphoma and leukaemia, IgG1), cetuximab (colorectal cancer, IgG1) and gemtuzumab (myeloid leukaemia, IgG4).[2]

The primary difference between the four human IgG subclasses lies in the hinge region. The hinge connects the Fab and Fc regions and is responsible for the flexibility of intact IgG molecules (see Supplementary Fig. S1). The upper hinge section

connects the Fab region to the cysteine-rich middle hinge section, while the lower hinge section connects the Fc region to the middle hinge.[3] Because of this inherent flexibility, crystal structures of full-length IgG antibodies are relatively few but include IgG1,[4,5] a hinge-deleted IgG1 mutant[6] and a murine IgG2a antibody.[7] Since antibody crystal structures only provide a single snapshot of the hinge region structure at best, antibody solution structures become important to assess conformational variability. Solution scattering and modeling studies have been presented for a human–mouse chimeric IgG4,[8] the bovine IgG1 and IgG2 subclasses,[9] the human IgA1 and IgA2 subclasses[10,11] and human IgD.[12] These studies revealed a versatile range of hinge structures and Fab–Fc orientations. Thus, human IgG4 displayed an asymmetric structure with the Fab arms close to the Fc region,[8] while the bovine IgG1 and IgG2 subclasses displayed extended hinge structures leading to a Y-shaped molecule.[9] Human IgA1 showed an extended hinge leading to a T-shaped antibody, while the shorter hinge of human IgA2 resulted in both T- and Y-shaped structures.[10,11] The long human IgD hinge is semiextended and leads to a T-shaped arrangement of the Fab and Fc fragments.[14] Thus, constrained scattering modeling based on known Fab and Fc crystal structures is a powerful means of establishing intact antibody structures in solution.

The interest of rabbit IgG is its single IgG subclass with an upper and a middle hinge length of only 11 residues.[13] Rabbit IgG has been the target of many classic antibody studies.[14,15] Rabbit IgG binds to complement C1q and FcRs, when human IgG4 with a similar upper and middle hinge length of 12 residues does not activate complement. To clarify this functional difference, we describe solution structure determinations for rabbit IgG by ultracentrifugation and scattering combined with constrained modeling, for comparison with our recent IgG4 study.[8] High-throughput X-ray scattering permits the rabbit IgG conformation to be readily measured in different salts during one beam session.[16] The newly developed SANS2D neutron instrument likewise permits rabbit IgG to be readily studied at different temperatures. Thus, antibody conformational changes can be studied under widely different solution conditions.[17] In contrast to human IgG4 that is monomeric, we show that rabbit IgG is mostly monomer but with significant proportions of buffer-dependent dimer and its monomer conformation is unchanged with buffer. The rabbit IgG monomer structure was determined by constrained scattering modeling. We show that its hinges are extended and that the Fab regions are positioned asymmetrically relative to the Fc region. The resulting molecular models showed that the binding of FcR and complement C1q to the top of the Fc region in rabbit IgG is permitted.

Results

Purification of rabbit IgG

Rabbit IgG was subjected to gel filtration to ensure that the protein was monodisperse immediately prior to ultracentrifugation or scattering experiments. This eluted as a symmetric main peak at 16 ml, which was preceded by a small peak at 14 ml that was attributed to minor dimer formation (Supplementary Fig. S2). The main peak showed a single band between 200 and 116 kDa in nonreducing SDS-PAGE that corresponds to the expected mass of 143.9 kDa for intact rabbit IgG molecule. Under reducing conditions, the heavy chains were observed at an apparent molecular mass of 55 kDa, and the light chains were between 31 and 21.5 kDa, both as expected (Supplementary Fig. S2).

Analytical ultracentrifugation of rabbit IgG

Sedimentation velocity experiments were performed in order to examine the monodispersity and shape of rabbit IgG between 0.5 and 5 mg/ml (3.5–35 μM). The SEDFIT analyses in six different buffers involved fits to as many as 500 scans, and the good agreement between the experimental boundary scans and fitted lines is clear (Fig. 1a–c). Only a major monomer peak at about 6.6 S and a smaller dimer peak at about 9.3 S were observed in all the size-distribution analyses $c(s)$. This monomer value agreed with that of 6.7 S reported for rabbit IgG previously, as well as a faster sedimenting species at 9.5 S that was likely a dimer.[14] These data showed that rabbit IgG was predominantly monomeric in solution, together with minor dimer formation.

The rabbit IgG monomer sedimented at slightly different rates in different buffers and temperatures at rotor speeds of 40,000 r.p.m. and 50,000 r.p.m. No significant difference in monomer $s_{20,w}$ value was recorded with rotor speed, and the data reported here are for 40,000 r.p.m.. The molecular masses of the monomer peak were measured as 146 ± 2 kDa (PBS-137), 144 ± 1 kDa (PBS-50), 147 ± 4 kDa (PBS-250), 145 ± 3 kDa (PBS-137 at 30 °C), 140 ± 8 kDa (PBS-137 at 5 °C) and 141 ± 9 kDa (PBS-137 in ^2H_2O), all of which agree well with the composition-calculated mass of 144 kDa (Materials and Methods). Extrapolation of the $s_{20,w}$ values to zero concentration gave similar monomer $s^\circ_{20,w}$ values of 6.62 S, 6.56 S and 6.56 S for the PBS-50, PBS-137 and PBS-250 buffers at 20 °C, respectively (Fig. 1d). The $s^\circ_{20,w}$ values were 6.62 S and 6.46 S at 5 °C and 30 °C in PBS-137, respectively. The change of 0.16 S between 5 °C and 30 °C is attributable to protein hydration changes at different temperatures, which in turn affects the partial specific volume v. In PBS-137 in heavy water, the monomer sedimented

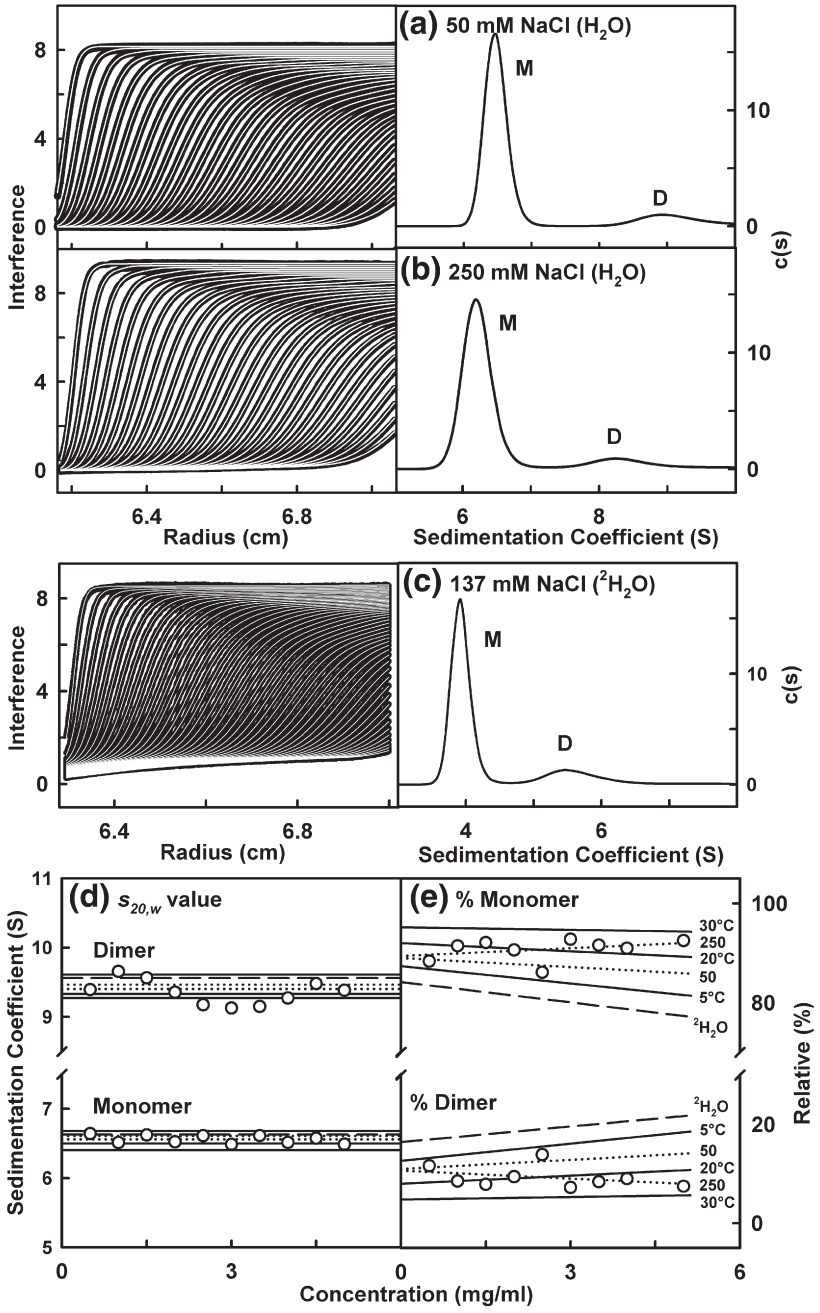

Fig. 1. Sedimentation velocity analysis of rabbit IgG. The experimentally observed sedimentation boundaries for (a) PBS-50, (b) PBS-250 and (c) PBS-137 in ^2H_2O were recorded at a rotor speed of 40,000 r.p.m. Thirty boundaries (black outlines) are shown from 150 scans, these being shown at intervals of every fifth scan for clarity, and these were fitted using SEDFIT as shown (white lines). The corresponding size-distribution analyses *c*(*s*) revealed monomer (M) and dimer (D) peaks at $s_{20,w}$ values of approximately 6.6 S and 9.3 S, respectively. (d) The concentration dependence of the $s_{20,w}$ values for peaks M and D are shown as a function of IgG concentration in the six buffers used in this study. (e) The percentages of monomer and dimer from integration of the *c*(*s*) analyses are shown for PBS-137 at 5 °C, 20 °C and 30 °C (continuous lines; labeled at the right); for PBS-50 and PBS-250 at 20 °C (dotted lines; labeled at the right) and for PBS-137 at 20 °C in heavy water (broken line). In (d) and (e), the 10 individual data points for PBS-250 are denoted as open circles to illustrate the reproducibility of the data points in each experiment.

at an apparent rate of 3.96 S (Fig. 1c), which, when corrected for the buffer density and viscosity of heavy water, resulted in an $s_{20,w}$ value of 7.09 S. Given that the *v* value for proteins is affected by the hydration shell[18,19] and the shell for heavy water will have a higher mass than that for light water, the *v* value will be reduced in 100% ^2H_2O. A *v* value of 0.7200 ml/g in place of 0.7306 ml/g gave a monomer $s^\circ_{20,w}$ value of 6.63 S close to that of 6.56 S for PBS-137. Interestingly, these $s^\circ_{20,w}$ values of 6.46–6.62 S are comparable with those reported for human IgG4 of 6.20–6.80 S.[8,20–22] The frictional coefficient ratio f/f_0 for rabbit IgG compares the frictional coefficient *f* for rabbit IgG by comparing this with the f_0 for a sphere of the same volume. From the f/f_0 value of 6.56 S for PBS-137 at 20 °C and the rabbit IgG composition, this ratio is computed as 1.32 for rabbit IgG. This is close to that of 1.30 for human IgG4 and indicates that rabbit IgG is as similarly compact in shape as human IgG4.[8]

The *c*(*s*) analyses revealed a minor $s_{20,w}$ peak at approximately 9.3 S, attributed to an IgG dimer that ranged between 5% and 25% of the total. The averaged $s_{20,w}$ value was similar at 9.46 ± 0.13 S (PBS-50), 9.27 ± 0.31 S (PBS-137) and 9.35 ± 0.18 S (PBS-250) at 20 °C. This was similar at

9.59 ± 0.15 S and 9.33 ± 0.16 S at 5 °C and 30 °C, respectively. In PBS-137 in heavy water, this was likewise similar at 9.56 ± 0.03 S. The corresponding molecular masses were 248 ± 6 kDa (PBS-50), 246 ± 10 kDa (PBS-137), 250 ± 8 kDa (PBS-250), 256 ± 13 kDa (PBS-137 at 30 °C), 244 ± 16 kDa (PBS-137 at 5 °C) and 241 ± 16 kDa (PBS-137 in ^2H_2O). These masses are comparable with the 288 kDa expected for a dimer. In order to determine the ratio of monomer to dimer, we performed integration of the *c*(*s*) peaks. In all buffers except PBS-250, the proportion of dimer increased with increasing IgG concentration (Fig. 1e). The level of dimer present was dependent on the NaCl concentration and temperature. For PBS-250, the level of dimer was constant at 9%. For PBS-137, the level of dimer increased from 8% to 11%. For PBS-50, the level of dimer increased from 11% to 16%. For PBS-137 at 30 °C, the least dimer was seen with an average of 5%. For PBS-137 at 5 °C, the most dimer was seen, where this increased from 12% to 20%. Large amounts of dimer were also seen for PBS-137 at 20 °C recorded in heavy water, when this increased from 18% to 25% for 2–7 mg/ml. These changes in dimer levels are consistent with both electrostatic and hydrophobic forces contributing toward dimer formation. In general, the observed changes were consistent with the reversibility of the monomer–dimer equilibrium. For example, the apparent dissociation constants K_D for this equilibrium ranged from 70 μM for PBS-137 at 20 °C in heavy water for the highest dimer formation to 350 μM in PBS-137 at 30 °C for the lowest dimer formation, as expected.

X-ray and neutron scattering of rabbit IgG

The solution structure of rabbit IgG was analyzed by X-ray scattering. X-rays were most effective for looking at the hydrated structure at 20 °C in a range of buffer salts. X-ray data collection was carried out between 0.5 and 5.0 mg/ml, using time-frame analyses to ensure the absence of radiation damage effects. Guinier analyses resulted in high-quality linear plots in three distinct regions of the *I*(*Q*) curves, as expected for antibodies, from which the R_G, $R_{XS\text{-}1}$ and $R_{XS\text{-}2}$ values were obtained within satisfactory $Q.R_G$ and $Q.R_{XS}$ limits (Fig. 2a and b). The X-ray R_G value for rabbit IgG in PBS-137 increased with concentration from 5.2 nm to 5.5 nm. An increase in R_G was not observed in PBS-250, with a mean R_G of 5.22 nm (Fig. 3a). These changes in R_G correspond with the observed changes in the *I*(0)/*c* values, where that for PBS-137 increased while that for PBS-250 was unchanged (Fig. 3b). Note that *I*(0)/*c* was much reduced in PBS-250 for reason of the reduced contrast difference between protein and buffer in this buffer. These findings concur with the changes in the monomer and dimer percentages seen by analytical ultracentrifugation (Fig. 1e), indicating that the increased R_G values can be explained by increased dimer formation (Fig. 3b). Each of the $R_{XS\text{-}1}$ and $R_{XS\text{-}2}$ values were almost unchanged between PBS-137 and PBS-250, with a mean $R_{XS\text{-}1}$ of 2.65 nm and 2.63 nm, respectively (Fig. 3c), and a mean $R_{XS\text{-}2}$ of 1.39 nm and 1.36 nm, respectively (Fig. 3d). This indicated that the change in the proportion of IgG dimer has no detectable effect on the IgG structure. In addition, these values are comparable to the $R_{XS\text{-}1}$ and $R_{XS\text{-}2}$ values of 2.56 nm and 1.40 nm, respectively, reported for human IgG4.[8]

Rabbit IgG in 100% ^2H_2O buffer was also analyzed by neutron scattering between 2.0 mg/ml and 7.0 mg/ml. Neutrons permitted the study of the unhydrated protein structure, where the hydration shell is almost invisible.[19] Neutrons were most useful for the study of temperature effects in PBS-137, these conditions being less readily accessible by X-ray scattering. The Guinier analyses revealed high-quality linear fits for the same three R_G, $R_{XS\text{-}1}$ and $R_{XS\text{-}2}$ parameters as described above for X-rays (Fig. 2c and d). The neutron R_G values increased with increasing concentration from 5.39 nm to 6.04 nm at 6 °C, from 5.21 nm to 5.87 nm at 20 °C and from 5.14 nm to 5.62 nm at 37 °C (Fig. 3e). The largest changes were seen at 6 °C. The changes seen with neutrons are comparatively large, indicating that the presence of heavy water promoted higher dimer formation. Extrapolation to zero concentration resulted in R_G values of 5.08 nm (6 °C), 5.01 nm (20 °C) and 4.99 nm (37 °C), these being less than the extrapolated R_G value of 5.22 nm seen by X-rays. The corresponding *I*(0)/*c* values also increased (Fig. 3f). The neutron $R_{XS\text{-}1}$ and $R_{XS\text{-}2}$ values showed almost no temperature dependence. The mean $R_{XS\text{-}1}$ values for 6 °C, 20 °C and 37 °C were 2.53 nm, 2.52 nm and 2.41 nm, respectively (Fig. 3g). The mean $R_{XS\text{-}2}$ values for 6 °C, 20 °C and 37 °C were 1.21 nm, 1.22 nm and 1.15 nm, respectively (Fig. 3h). The R_G, $R_{XS\text{-}1}$ and $R_{XS\text{-}2}$ values were slightly less than those seen by X-rays, and this is attributed to the near invisibility to neutron scattering of the surface hydration shell in heavy water.[19]

The distance distribution function *P*(*r*) provides structural information on IgG in real space. From the X-ray *P*(*r*) analysis, the R_G values for rabbit IgG in PBS-137 and PBS-250 were determined to be similar to those from the X-ray Guinier analyses, showing that the two analyses were self-consistent (filled and open symbols in Fig. 3a). The maximum length *L* of rabbit IgG was determined from the value of *r* when the *P*(*r*) curve intersects 0 to be between 16 nm and 17 nm for both PBS-137 and PBS-250 (Fig. 4a). The maxima in the *P*(*r*) curves correspond to the most frequently occurring interatomic distances within the structure. For rabbit IgG, two peaks, *M1* and *M2*, were identified in all the *P*(*r*)

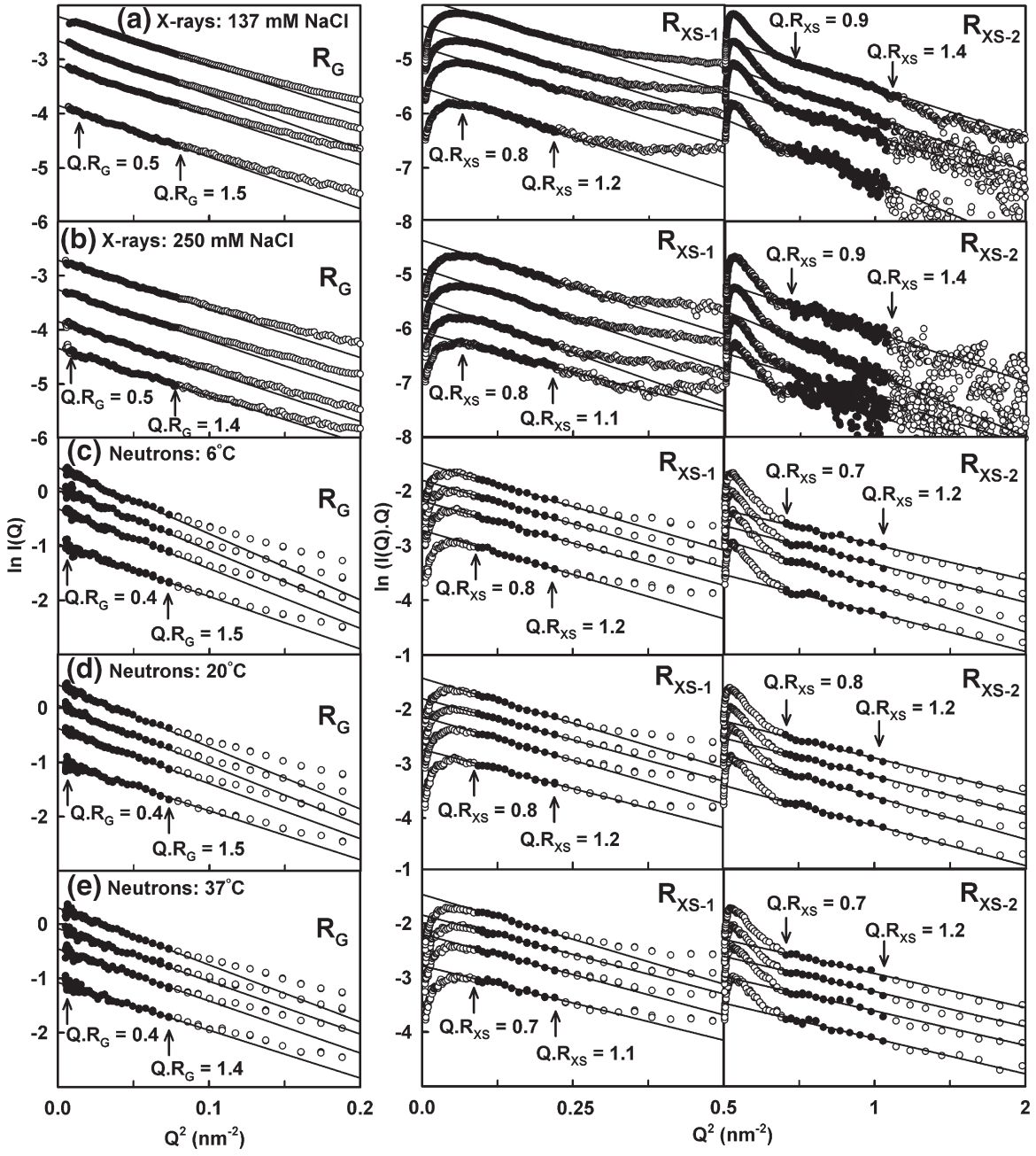

Fig. 2. X-ray and neutron Guinier R_G and R_{XS} analyses for rabbit IgG. (a and b) The X-ray scattering curves are shown for concentrations of 5, 3, 2 and 1 mg/ml from top to bottom, with those for PBS-137 at 20 °C in (a) and those for PBS-250 at 20 °C in (b). The filled circles between the arrowed data points represent the $Q.R_G$ and $Q.R_{XS}$ ranges used to determine the R_G and R_{XS} values. The Q range used for the R_G values was 0.09–0.28 nm^{-1} and those for the R_{XS-1} and R_{XS-2} values were 0.31–0.47 nm^{-1} and 0.65–1.04 nm^{-1}, respectively. (c–e) The neutron scattering curves are shown for concentrations of 7, 5, 3.5 and 2 mg/ml from top to bottom for rabbit IgG in PBS-137 in heavy water. (c) Data at 6 °C. (d) Data at 20 °C. (e) Data at 37 °C. The Q range used for the R_G values was 0.07–0.28 nm^{-1} and those for the R_{XS-1} and R_{XS-2} values were 0.31–0.47 nm^{-1} and 0.65–1.04 nm^{-1}, respectively.

curves at approximately 5 nm and 8 nm, respectively. No clear shift in the positions of peaks *M1* and *M2* was observed with concentration or buffer. Because the two peaks are sensitive to the arrangement of the Fab and Fc regions within IgG, the lack of change indicated that the solution arrangement of Fab and Fc within rabbit IgG is similar in different buffers. In comparison with the equivalent data for human IgG4, the human *L* values are closely similar; however, the human peaks *M1* and *M2* shift with protein

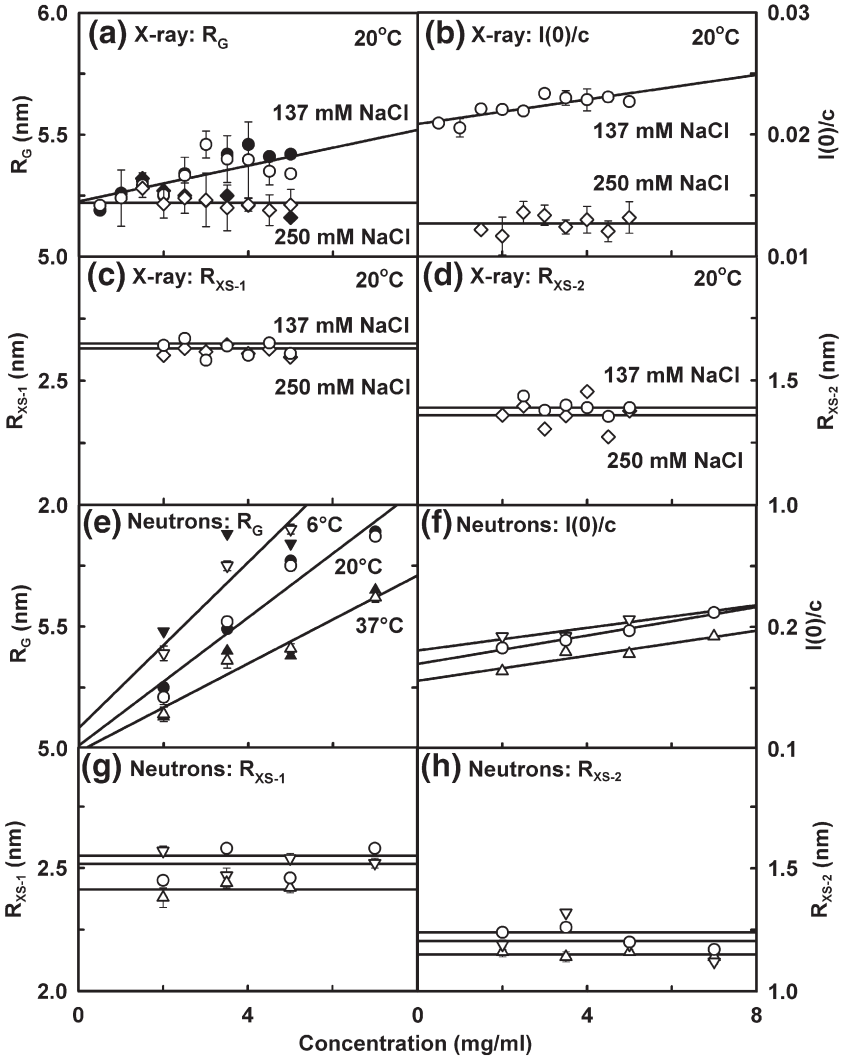

Fig. 3. Concentration and temperature dependence of the X-ray and neutron Guinier values for rabbit IgG. (a–d) The X-ray values were each measured in quadruplicate and averaged. Linear regression fits give the mean ± SD (in some cases, the error bars were smaller than the symbol). (a) The X-ray R_G values are shown for PBS-137 [(○) and (●)] and PBS-250 [(◊) and (◆)]; the open symbols correspond to the Guinier values and the filled symbols correspond to the $P(r)$ values. (b) The corresponding X-ray $I(0)/c$ values are shown for PBS-137 (○) and PBS-250 (◊). (c and d) The X-ray R_{XS-1} and R_{XS-2} values are shown for PBS-137 (○) and PBS-250 (◊), with the fitted lines for the R_{XS-1} and R_{XS-2} values being the mean value. (e–h) The neutron values each correspond to a single measurement in PBS-137 in heavy water. The fitted lines correspond to linear regression fits. (e) The R_G values at 6 °C [(▽) and (▼)], 20 °C [(○) and (●)] and 37 °C [(△) and (▲)], with the open symbols corresponding to the Guinier values and the filled symbols corresponding to the $P(r)$ values. (f) The corresponding $I(0)/c$ values are shown for 6 °C (▽), 20 °C (○) and 37 °C (△). (g and h) The R_{XS-1} and R_{XS-2} values are shown for 6 °C (▽), 20 °C (○) and 37 °C (△). The fitted lines shown for the R_{XS-1} and R_{XS-2} values are the mean values.

concentration (0.3–1.2 mg/ml) in PBS-137 that indicated non-ideality in the solution properties of human IgG4.[8]

The neutron $P(r)$ analysis showed that the R_G values for rabbit IgG in PBS-137 at 6 °C, 20 °C and 37 °C increased with increasing concentration (Fig. 3e). The R_G and $I(0)/c$ values indicated a temperature dependence, which is attributable to the amount of dimer formed. This is consistent with the sedimentation velocity experiments where dimer formation depended on the temperature and the presence of heavy water (Fig. 1e). The observed L values were between 17 nm and 21 nm for PBS-137 at 6 °C, 16 nm and 20 nm at 20 °C and 16 nm and 17 nm at 37 °C (Fig. 4b). These L values showed that the greater proportions of dimer at lower temperatures resulted in measurably increased dimensions. Because dimer is present in low amounts and the L values are not precisely measured, it is likely that the maximum length of the dimer is larger than 21 nm. As with the X-ray $P(r)$ curves, two peaks *M1* and *M2* were identified at approximately 5 nm and 8 nm, respectively, in the neutron $P(r)$ curves. No change was identified in the positions of *M1* and *M2* with changing concentration, indicating no difference in the internal Fab–Fc arrangement within rabbit IgG.

Starting model for rabbit IgG

In order to determine the rabbit IgG solution structure, we constructed a starting model from the crystal structures of the Fab fragment [Protein Data Bank (PDB) code 3NL4] and the Fc fragment (PDB code 2VUO) and molecular models for the hinge. The full hinge itself is formally defined by the 19-residue 220-APSTCKSPTCPPPELLGGP-238.[13]

(i) The rabbit Fab crystal structure has all its residues present in the light chain and up to Cys224 in the heavy chain (Supplementary Fig. S3a–e). Even though the Fab region

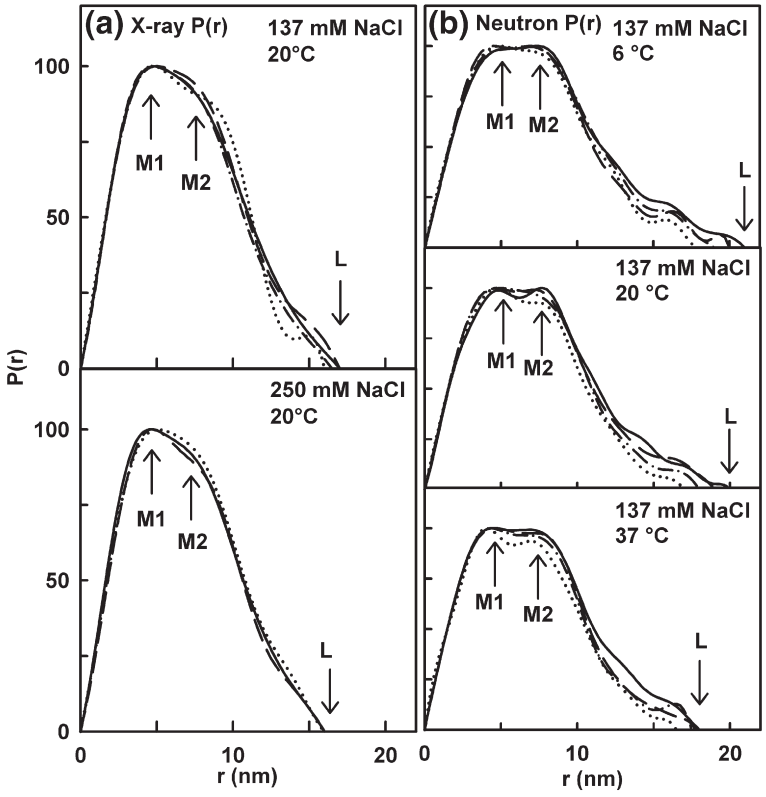

Fig. 4. X-ray and neutron distance distribution analyses $P(r)$ for rabbit IgG. The peak maxima at *M1* and *M2* are indicated by arrows. The maximum length is denoted by *L*. (a) The X-ray $P(r)$ curves for PBS-137 and PBS-250 are shown. The four curves for 1, 2, 3 and 5 mg/ml are denoted as dotted, dot/dash, broken and continuous lines in that order. That for 1 mg/ml in PBS-250 is not shown. (b) The neutron $P(r)$ curves for PBS-137 in ^2H_2O buffer are shown. The four curves for 2, 3.5, 5 and 7 mg/ml are denoted by dotted, dot/dash, broken and continuous lines in that order.

formally terminates at Val219, Cys224 forms an intrachain disulfide bond within the C_H1 domain (Supplementary Fig. S1). It was therefore assumed that the location of residues Ala220 to Cys224 was well represented by the Fab crystal structure.

(ii) The rabbit Fc structure was based on interpretable density for residues Pro230 to Ser444 (Supplementary Fig. S3e–g). While atomic coordinates were present up to Pro230 (chain A) and Pro231 (chain B), the missing side chains for residues Pro231, Pro232, Glu233 and Leu235 in chain B were added using Discovery Studio. Pro230 was deleted from chain A so that both chains started at Pro231. Although the Fc region formally starts at Ser239, the lower hinge residues between Pro232 and Pro238 were considered to be well represented by the crystal structure. The two complex-type oligosaccharide chains at Asn297 in the C_H2 domains were visible as biantennary oligosaccharides with a $Man_3GlcNAc_2$ core and two GlcNAc.Gal antennae. These were not modified for the modeling. In one chain, one of the two GlcNAc antennae is absent. The two oligosaccharides at Asn297 cover a hydrophobic patch on the C_H2 domain surface and extend into the cavity between the two C_H2 domains.[15]

(iii) The full hinge is characterized by six proline residues and one Cys229 interchain disulfide bridge within 19 residues. Because Pro230 (chain A) and Pro231 (chain B) are 0.780 nm apart in the Fc region, this is consistent with the Cys229–Cys229 disulfide bridge in the hinge.[17] Because only six residues are missing in this region in the two crystal structures (Supplementary Fig. S3e), it was deduced that hinge variability would be well modeled by conformational sampling of an eight-residue peptide composed of the upper hinge sequence 225-SKPTCP-230 and flanked by the two terminal residues Cys224 and Pro231 that were used as anchor points in the Fab and Fc crystal structures (Supplementary Fig. S3e). A total of 5000 randomized hinge sequences were generated. Because this sequence 224-CSKPTCPP-231 is located asymmetrically in the Fc structure, this meant that the intact rabbit IgG structure will not have 2-fold axial symmetry about the Fc fragment.

Search fit for the rabbit IgG solution structure

In order to model the rabbit IgG solution structure, we assembled a total of 5000 rabbit IgG conformationally randomized structures from the Fab and Fc

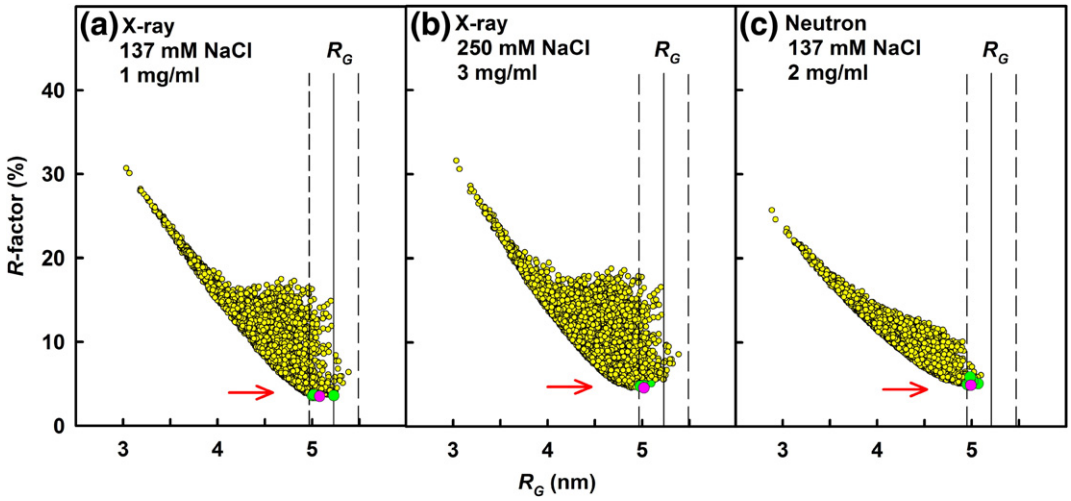

Fig. 5. Constrained modeling analyses for rabbit IgG. The 5000 goodness-of-fit *R*-factors are compared with the corresponding calculated X-ray and neutron R_G values for a conformationally randomized set of (a and b) hydrated (X-ray) and (c) unhydrated (neutron) rabbit IgG models. The 10 best-fit models with the lowest *R*-factors are shown in green, of which the best-fit model is shown in pink. The experimentally observed R_G values are shown by vertical lines as labeled with error ranges of ±5% to follow the Guinier R_G values in Table 1. (a) X-ray models compared with 1 mg/ml IgG in PBS-137; (b) X-ray models compared with 3 mg/ml IgG in PBS-250; (c) neutron models compared with 2 mg/ml IgG in PBS-137 in ^2H_2O.

crystal structures and the library of randomized hinge peptides of length 2.75–2.8 nm (Materials and Methods). Following calculation of the scattering curves from these, we compared each curve with the experimental X-ray and neutron curves. The experimental scattering curves selected for fits corresponded to the lowest concentrations in order to reduce the dimer content (Fig. 1e). For the X-ray scattering curves, the 1-mg/ml scattering curve in PBS-137 and the 3-mg/ml scattering curve in PBS-250 were used. For the neutron scattering curve, the 2-mg/ml scattering curve in PBS-137 in heavy water was used. The fits were assessed in Fig. 5. There, the identification of a single minimum *R*-factor value showed that the modeling strategy had successfully generated a single family of solution structures for rabbit IgG starting from a wide range of orientations and translations of the two Fab and Fc fragments. When the goodness-of-fit *R*-factors were compared with the R_G values, the lowest *R*-factors in the 5000 curve fits corresponded to models with R_G values close to the experimental R_G values, as desired (Fig. 5).

Filters based on the experimental scattering data were used to reject unsatisfactory models and identify the best-fit models.

(i) A ±5% filter for steric overlap eliminated the models in which the Fab and Fc regions and the hinge sterically overlapped with each other as the result of inappropriate hinge conformations. In order to correspond to the composition-calculated volume of rabbit IgG, satisfactory sphere models needed a minimum total number *N* of 1470 spheres for the hydrated X-ray models and 1136 spheres for the unhydrated neutron models.

(ii) A ±5% filter of the modeled R_G values that were calculated from the same Guinier *Q* ranges used for the experimental X-ray or neutron R_G values identified the models that fitted the degree of elongation determined by X-rays or neutrons.

(iii) When the models were ordered starting from their lowest *R*-factors, 10 best-fit models for rabbit IgG were identified. These best-fit models are found as a single cluster (green in Fig. 5), again suggesting that a single conformationally related best-fit family of structures has been identified. In terms of the Cys229–Cys229 inter-heavy-chain disulfide bridge, the C^{α} separations between the two Cys229 residues should be between 0.4 and 0.75 nm.[23] This separation in the 30 best-fit models was between 0.83 and 2.11 nm, being satisfactory. Visual inspection of the best-fit models showed that the two Cys229 residues were in proximity to each other as desired, although a crystal structure will be required to define the location of the Cys229–Cys229 disulfide bridge.

The final outcome of the modeling showed good visual curve fits in all three cases, both for the experimental *I*(*Q*) curves and the *P*(*r*) curves shown as insets (Fig. 6). Slight deviations seen at

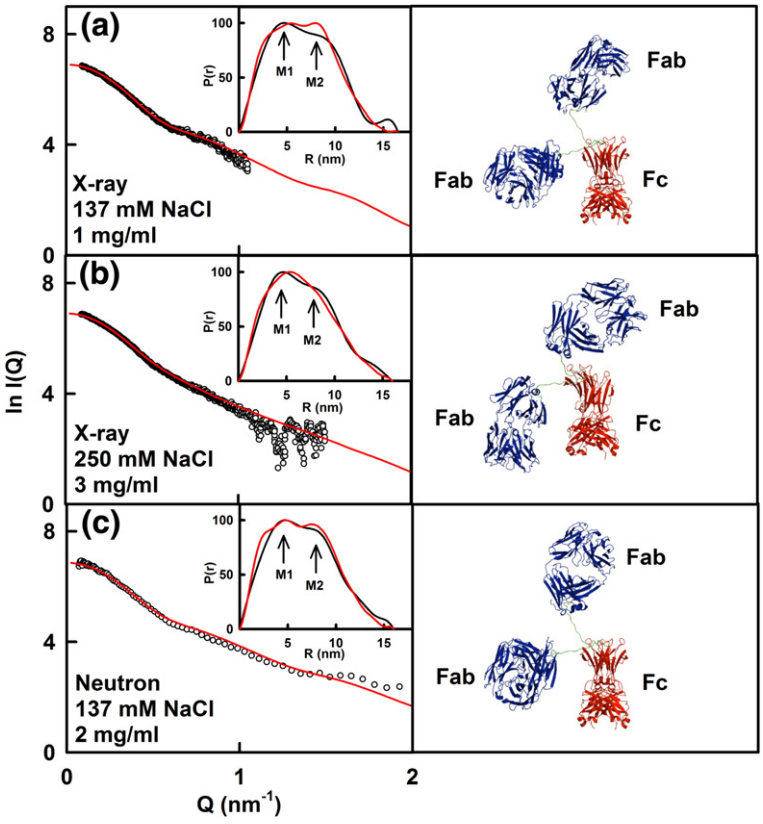

Fig. 6. X-ray and neutron scattering curve fits for the best-fit monomer IgG models. The fits correspond to (a) 1 mg/ml rabbit IgG in PBS-137 by X-ray scattering, (b) 3 mg/ml rabbit IgG in PBS-250 by X-ray scattering and (c) 2 mg/ml rabbit IgG in PBS-137 in $^{2}H_2O$ by neutron scattering. In the left-hand panels, the experimental data are indicated by circles (black) and the modeled best-fit scattering curve is indicated by the continuous line (red). The insets correspond to the experimental (black) and best-fit modeled (red) *P*(*r*) curves, in which the *M1* and *M2* values are indicated by arrows. In the right-hand panels, the best-fit rabbit IgG models are shown, with the Fab regions in blue and the Fc regions in red. The Fc region is shown in the same orientation in all three models.

low *Q* for the neutron fit are consistent with the presence of small amounts of dimer (Fig. 6c). In each case, the R_G values for the 10 best-fit models were within acceptable error of the experimental values (Table 1). The three models in Fig. 6 displayed similar asymmetric arrangements of the two Fab regions compared to the Fc region in all three buffers as being the most consistent with the fits. The three *R*-factor values for the best-fit model (pink in Fig. 5) were acceptable at 3.5%, 4.6% and 4.9%, respectively, for PBS-137, PBS-250 and PBS-137 in heavy water. These values are low when compared with those from other similar modeling fits.[24]

Sedimentation coefficient modeling of the rabbit IgG monomer and dimer

The $s_{20,w}$ values of each of the three sets of 10 best-fit scattering rabbit IgG models were calculated for comparison with the experimental values of 6.56 S for the IgG monomer (Fig. 1d). The 30 $s_{20,w}$ values for the best-fit hydrated sphere models ranged from 6.47 S to 6.74 S using HYDRO (Table 1). The corresponding sets of 30 $s_{20,w}$ values using HYDRO-PRO ranged from 6.13 S to 6.48 S (Table 1). Given that the calculations are generally accurate to within ±0.21 S,[24] both sets of $s_{20,w}$ values agree well with the experimental value of 6.56 S.

In order to assess the presence of dimer in the scattering curve fits, we generated dimer structures starting from the best-fit monomer structure for PBS-137. While holding one monomer fixed, a second identical monomer was positioned against this in variable positions. Models included face-to-face structures of Fab–Fc pairs (Fig. 7a), tip-to-tip structures involving a single Fab–Fab contact (Fig. 7b) or bivalent Fab–Fab or Fab–Fc contacts (Fig. 7c). This variety encompassed the most extended and most compact structures possible. For each model, the calculated $s_{20,w}$ value was compared with the experimental $s_{20,w}$ value of 9.27 S for the dimer. The dimer models with bivalent Fab contacts gave an $s_{20,w}$ value of 9.4 S using HYDROPRO.

Effect of dimer on the X-ray and neutron curve fits

Up to here, the scattering curve fits had assumed that the rabbit IgG scattering curve corresponded to monomer only. The dimer peak observed in the sedimentation *c*(*s*) analyses showed that 5–25% of dimer was present (Fig. 1e). Even though the scattering curves with the lowest dimer concentrations were used for fits, each curve fit in Fig. 6 was reevaluated for the presence of dimer. The scattering curves for mixtures of the monomer and dimer

Table 1. Modeling searches of the X-ray and neutron scattering and sedimentation coefficient data for rabbit IgG

	Filter	Models	Spheres[a]	R_G (nm)[b]	R_{XS-1} (nm)	R_{XS-2} (nm)	D_{max} (nm)	*R*-factor (%)	$s_{20,w}$ (S)[c]
X-ray fit, 1 mg/ml, PBS-137	None	5000	1099–1509	3.03–5.39	0.36–2.98	0.26–2.68	n.a.	3.5–30.7	n.a.
	R_G, R_{XS-1}, *R*-factor	10	1452–1485	5.00–5.23	2.66–2.82	1.24–1.40	n.a.	3.5–3.7	6.53–6.67; 6.26–6.48
	Best fit	1	1471	5.08	2.76	1.25	16.5	3.5	6.61; 6.36
Experimental data	n.a.	n.a.	n.a.	5.24±0.12; 5.26±0.12	2.52±0.19	1.32±0.07	16	n.a.	6.56
X-ray fit, 3 mg/ml, PBS-250	None	5000	1099–1509	3.03–5.39	0.36–2.98	0.26–2.68	n.a.	4.6–31.6	n.a.
	R_G, R_{XS-1}, *R*-factor	10	1453–1481	4.98–5.05	2.58–2.79	1.20–1.41	n.a.	4.6–5.1	6.66–6.74; 6.25–6.45
	Best fit	1	1481	5.02	2.58	1.41	16	4.6	6.66; 6.25
Experimental data	n.a.	n.a.	n.a.	5.23±0.11; 5.23±0.09	2.62±0.08	1.31±0.22	16	n.a.	6.56
Neutron fit, 2 mg/ml, PBS-137	None	5000	903–1151	2.88–5.09	0.12–2.62	0.64–2.41	n.a.	4.9–25.7	n.a.
	R_G, R_{XS-1}, *R*-factor	10	1118–1138	4.96–5.01	2.33–2.62	1.13–1.53	n.a.	4.9–5.9	6.47–6.56; 6.13–6.32
	Best fit	1	1121	4.99	2.52	1.16	16	4.9	6.51; 6.30
Experimental data	n.a.	n.a.	n.a.	5.21; 5.25	2.45	1.24	17	n.a.	6.63

[a] The optimum number of unhydrated and hydrated spheres predicted from the sequence is 1136 and 1470, respectively.
[b] The first experimental value is from the Guinier R_G analysis (Fig. 2) and the second one is from the GNOM *P*(*r*) analysis (Fig. 4).
[c] The first modeled value corresponds to that from HYDRO and the second one is from HYDROPRO.

structures (Figs. 6a and 7c) were summed from 0% to 100% in 1% increments.[25] The extent of change in the normalized scattering curve is summarized in Fig. 7d. The 101 summed curves were compared with each of the three fits in Fig. 6. For PBS-137 (Fig. 6a), the *R*-factor improved from 3.5% to 3.4% when 3–11% of dimer was included in the monomer curve fit. This proportion agreed well with the 8% dimer observed in the *c*(*s*) fit (Fig. 1e). For PBS-250 (Fig. 6b), the *R*-factor improved from 4.6% to 3.7%

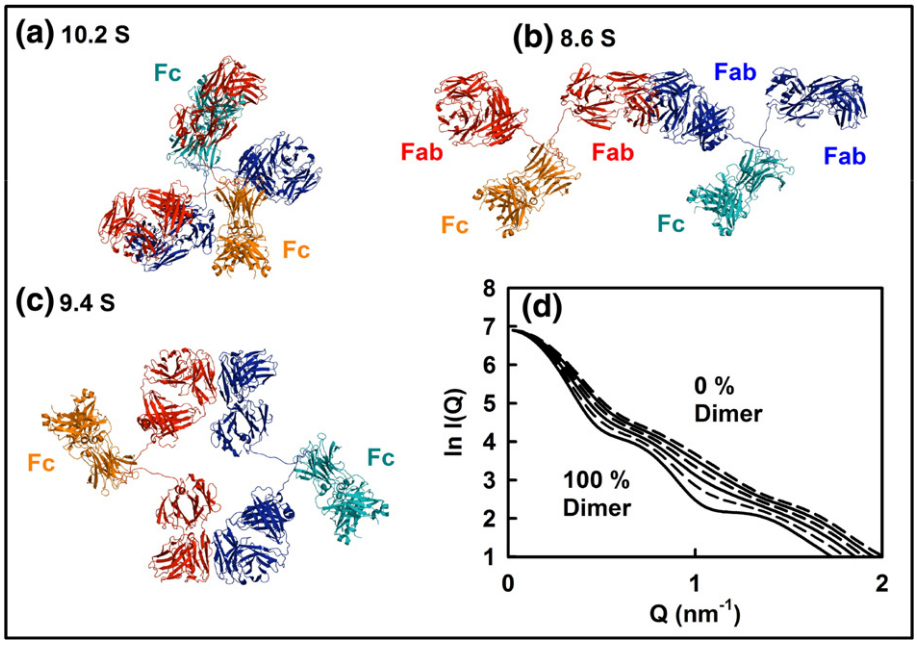

Fig. 7. Dimer structures of rabbit IgG. Three trial IgG dimer structures and their sedimentation coefficients determined by HYDROPRO are shown. (a) Compact dimer structure with a calculated $s_{20,w}$ value of 10.2 S formed by face-to-face contacts between two Fab–Fc pairs. (b) Extended dimer structure with a calculated $s_{20,w}$ value of 8.6 S formed by Fab-to-Fab tip-to-tip contacts. (c) Intermediate dimer structure with a calculated $s_{20,w}$ value of 9.4 S formed by two Fab-to-Fab contacts. (d) Calculated X-ray scattering curves for the sum of monomer and dimer that correspond to 0–100% monomer with 100%, 80%, 60%, 40%, 20% and 0% dimer. For monomer 1, Fc is shown in orange and Fab is shown in red; for monomer 2, Fc is shown in cyan and Fab is shown in blue.

when 14–22% of dimer was included in the curve fit. This proportion compared well with the 7% dimer observed in the *c*(*s*) fit (Fig. 1e). For PBS-137 with heavy water (Fig. 6c), the *R*-factor was improved from 4.9% to 4.0% when 17–26% of dimer was included in the curve fits. This proportion agreed well with the 18% dimer observed in the *c*(*s*) fit (Fig. 1e). The improvements seen in all three cases, in particular, for the neutron fit, showed that the inclusion of 7–18% dimer in the fits had no discernible effect on the reliability of the X-ray and neutron curve fits.

Effect of IgG composition on the X-ray and neutron curve fits

Rabbit IgG is heterogeneous with respect to its V_H and V_L complementarity-determining regions, light-chain isotypes, allotypic differences in the H and L chains and its glycosylation. Because the structural modeling focused on the hinge conformation and because rabbit IgG has a single subclass, the length of the hinge region is the same in all molecules. Thus, the scattering modeling was effective. In relation to amino acid and glycosylation differences, these were considered as follows:

(i) Polyclonal rabbit IgG will include the *d* and *e* allotypes, which correspond to single amino acid substitutions in the C_H2 domain and are expected to have little effect on the curve fits. The multiple substitutions in the *a* allotype affect over 10% of the framework residues in the V_H domain.[26,27] Those in the *b* allotype affect up to 40% of the residues in the LC κ domain.[28–30] The κ light chain has two isotypes K1 and K2 with approximately 70–90% being the K1 isotype.[31–33] These residue changes are outside the hinge region and are not expected to affect the scattering fit modeling.

(ii) In relation to the asymmetric hinge O-linked glycosylation at 40% occupancy,[34] the glycosylation site is Thr228 in the hinge (Supplementary Fig. S3). Thr228 can be substituted with Met, Pro or Leu, thus reducing the glycosylation. The effect of an O-linked glycosylation in the best-fit model was tested by adding a NeuNAc.Gal.GalNAc trisaccharide to one Thr228 site. The *R*-factors were unchanged at 3.5% for the 54–100% of the curves that corresponded to one added O-linked trisaccharide. They were almost unchanged at 3.6% for the 0–53% of the curves that corresponded to the added trisaccharide. This lack of change is likewise not expected to affect the scattering modeling.

Discussion

Rabbit IgG structure and function

We have determined the first view of an asymmetric antibody conformation in solution for rabbit IgG that revealed new insights into its function, most notably its interactions with the FcR and with complement C1q (Fig. 8). Crystal structures often do not provide information about the arrangements of the three Fab and Fc regions within the intact antibody. Here, we show that the two Fab regions are asymmetrically arranged about the Fc region in rabbit IgG. This solution structure has implications for FcR and C1q binding to IgG, both of which are important for effector responses within the immune system.

In distinction to other species (e.g., human, mouse, rat), the rabbit immune system utilizes a single IgG subclass. The four IgG subclasses in human, rat and mouse arose from gene duplication events. These different IgG subclasses may be produced differentially in response to different pathogen exposures. The mean serum concentration of rabbit IgG is 13.6 mg/ml (a range of 12.0–14.5 mg/ml).[35] The mean serum concentration of human IgG is similar at 13.2 mg/ml, being composed of 8 mg/ml for IgG1 (a range of 5–12 mg/ml), 4 mg/ml for IgG2 (2–6 mg/ml), 0.8 mg/ml for IgG3 (0.5–0.1 mg/ml) and 0.4 mg/ml for IgG4 (0.2–1 mg/ml).[1] Rabbit IgG is able both to activate complement and to bind to FcγRs. Some human IgG subclasses show reduced activation via C1q or FcγR binding.[1] In the human immune system, the FcγI receptor type has high affinity and is activated by monomeric IgG, while FcγII and FcγIII are low-affinity receptors and require multivalent immune complexes for activation. The FcγRs also differ in their IgG specificities, with FcγIII binding IgG1 and IgG3 more tightly than IgG2 and IgG4.[36,37]

Hinge structure of rabbit IgG

The X-ray and neutron scattering modeling showed that the rabbit IgG hinge is extended in solution and that the arrangement of the Fab and Fc regions is unaffected by different concentrations or buffers. The resulting asymmetric solution structure for rabbit IgG is the consequence of its comparatively short hinge sequence compared to the four human subclasses (Supplementary Fig. S3h). The rabbit IgG hinge is too short to permit the three Fab and Fc regions to exhibit unrestricted conformational freedom about the hinge. The upper hinge in rabbit IgG is nine residues long, compared with the seven in that of human IgG4. However, the first five hinge residues (Ala220 to Cys224) are incorporated within the Fab region, being terminated by Cys224 that

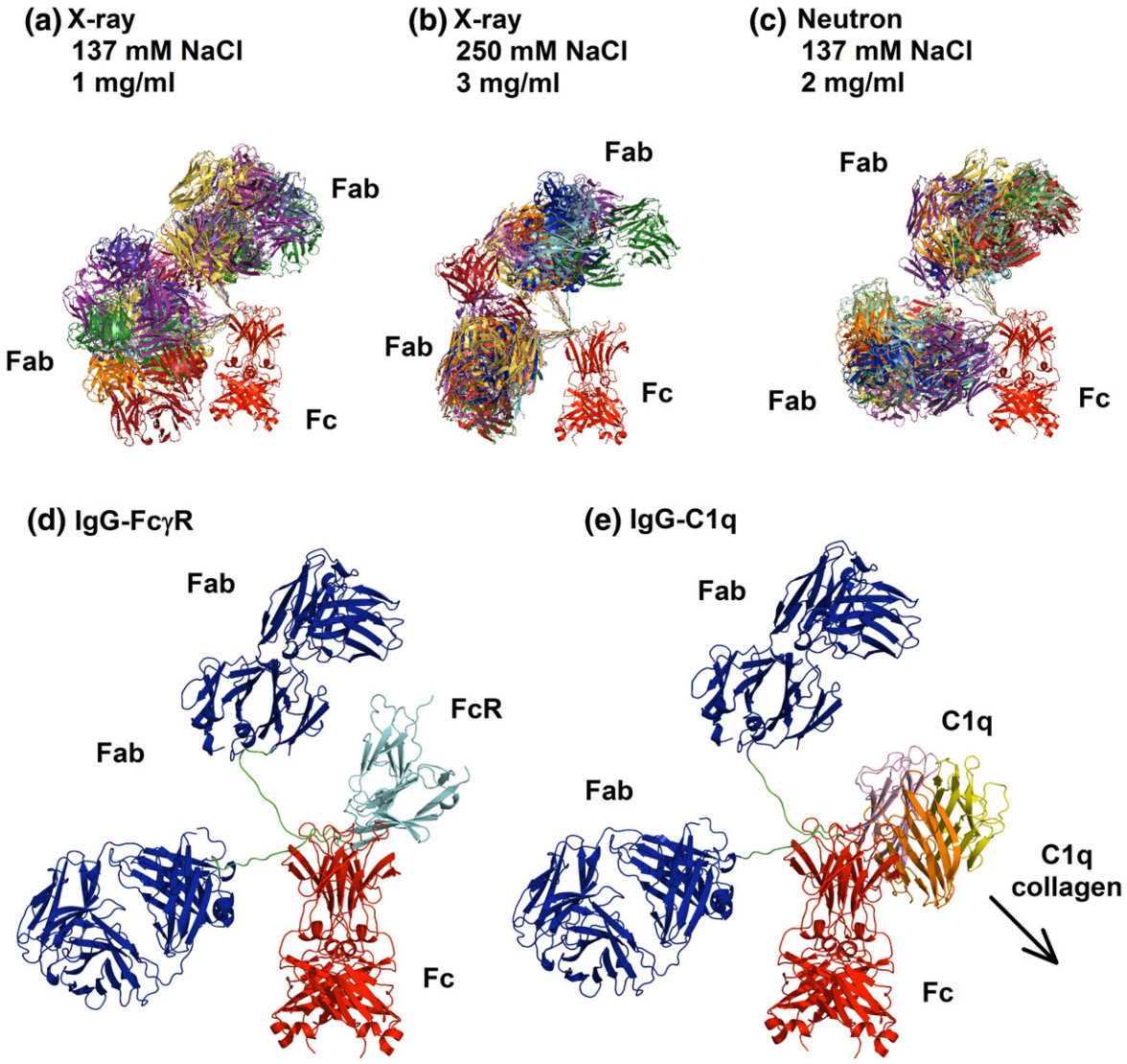

Fig. 8. The best-fit rabbit IgG models and their interactions with the FcR and a C1q globular head. The 10 best-fit models from each analysis are shown superimposed upon their Fc region (red). These correspond to (a) 1 mg/ml IgG (X-rays) in PBS-137 (PDB code 4GDQ), (b) 3 mg/ml IgG (X-rays) in PBS-250 (PDB code 4GDR) and (c) 2 mg/ml IgG (neutrons) in PBS-137 in $^{2}H_{2}O$ (PDB code 4GDS). (d) The best-fit IgG model from (a) is shown superimposed with the crystal structure for the Fc (red)–FcγRIII (cyan) complex (PDB code 1E4K). Both the rabbit Fc and human Fc structures are shown overlaid upon each other. Other Fc–FcR crystal structures (PDB codes 1T83 and 1T89) give very similar views. (e) The best-fit IgG model from (a) is shown superimposed with the crystal structure for C1q (PDB code 1PK6) according to Table 2 of a docking prediction for this complex.[44] For C1q, the A chain is colored yellow, the B chain is colored orange and the C chain is colored pink. The approximate location of the collagen triple helix in C1q pointing away from the C1q head is shown by the black arrow.

forms an intrachain disulfide bond within the C_H1 domain. The middle hinge is characterized by interchain disulfide bonds that are responsible for the rigidity of the middle hinge. Rabbit IgG has only two residues in the middle hinge and one interchain disulfide bridge, while human IgG4 has a middle hinge of five residues and two interchain disulfide bridges. The rabbit IgG upper and middle hinge has to be structurally extended to accommodate its Fab and Fc regions. To illustrate this, we redefined the hinge length used in the conformational searches (224-CSKPTCPP-231) by the C^{α} positions of the flanking residues Thr223 and Pro232. The maximum possible length of nine extended peptides is 3.2 nm. The 10 best-fit structures gave hinge lengths between 3.16 and 3.37 nm for PBS-137, 3.14 and 3.33 nm for PBS-250 and 3.09 and 3.44 nm for PBS-137 in heavy water. This showed that good fits to the X-ray and neutron data were obtained only with fully extended hinge structures.

The solution structure of rabbit IgG is similar to that for human IgG4 determined by less extensive X-ray scattering data and modeling.[8] Like the rabbit IgG solution structure, the human IgG4 solution structure was asymmetric with one Fab–Fc pair closer together than the other pair. The length of the upper and lower hinges is one residue longer in human IgG4 than in rabbit IgG (Supplementary Fig. S3h). Intriguingly, unlike rabbit IgG, human IgG4 showed internal conformational changes with dilution in PBS-137. The hinge length increased slightly with decreasing concentration, accompanied by a decreased separation between the Fab–Fc regions. These conformational changes were recently reconfirmed with a different human IgG4 (G.-K.H., L.R., P.A.D. and S.J.P., unpublished results).

Interactions with FcR

FcR binding to IgG activates antibody-dependent cell-mediated cytotoxicity events. FcRs are antibody class-specific, with the FcγR group interacting with the IgG class. FcγRs are type I transmembrane glycoproteins consisting of extracellular and cytoplasmic regions. The extracellular regions bind to antibody and exhibit a high degree of sequence identity between different FcγRs; however, the cytoplasmic domains differ significantly.[36] This explains the diverse functions of FcγRs including activating, inhibitory and synergistic effects with some containing immunoreceptor tyrosine-based activation or inhibition motifs.[38] The extracellular region of FcγR contains either two or three C2-type immunoglobulin-like domains (designated as D1, D2 and D3). Different FcγRs have different subclasses, with subclasses A, B and C known for human FcγRI and FcγRII and subclasses A and B known for human FcγRIII.[39] In the Fc region, 60% of the interactions with the FcγRs are mediated through residues Leu234–Pro238 of the lower hinge region, these residues being identical in human IgG1 and rabbit IgG (Supplementary Fig. S3h).[37] The interaction involves predominantly the BC, C′E and FG loops of the D2 domain and its C′ β-strand and the hinge loop between D1 and D2.[38] The interactions involve van der Waals contacts and hydrogen bonds, mostly from the Fc residues Leu234–Pro238 and the FcγR residues Thr113, Ala114 and Val155–Lys158. The detailed interaction is shown in Fig. 4 of the crystal structure study.[40] The Fc residue Pro329 forms a proline sandwich with the FcγR residues Trp87 and Trp110.[40] Fc glycosylation also plays a role. The oligosaccharides at Asn297 stabilize the Fc structure, and differences in this Fc glycosylation may alter the Fc–FcγR interactions.[41,42]

The IgG–FcγR interaction is clarified by our IgG solution structures. Molecular views of the superimposed best-fit rabbit IgG models show that the Fab regions are positioned at the top of the Fc region and along one Fc face to leave the other Fc face exposed (Fig. 8a–c). The accessibility of the lower hinge in rabbit IgG is demonstrated by overlaying the best-fit models with three crystal structures of the Fc–FcR complex (Fig. 8d).[40,43] Complex formation is enabled by the asymmetric IgG structure. The crystal structure of rabbit Fc showed that the lower hinge has an acute bent conformation even in the absence of receptor.[15] Here, we show that this lower hinge bend in Fc indeed resulted in the displacement of the Fab regions in intact rabbit IgG to permit FcγR interactions with the top of the Fc region.

The reactivity of complement C1q with the four human IgG subclasses varies, this being presumed to be mediated by steric interference from the Fab arms in the approach of C1q to the C_H2 sites, in which the affinities decrease in the sequence IgG3 > IgG1 > IgG2 > IgG4.[1] This sequence also reflects the complement fixation ability of the four subclasses,[1] where human IgG4 does not activate complement. The C1q binding site occurs also at the top of the C_H2 domain in the Fc region. The Fc residues Glu318, Lys320 and Lys322 are often implicated as the core residues for C1q binding, and Pro329 and Pro331 are also important (Supplementary Fig. S3f). Mutagenesis has implicated ArgA162, ArgB108, HisB117, ArgB129, ArgB163 and ArgC156 on the A, B and C chains of C1q in the interaction.[44] The interaction between complement C1q and IgG Fc is yet to be crystallographically examined. The prediction of docking models for the Fc–C1q interaction suggested that the B and C chains of the C1q head interacted with the top of both C_H2 domains in the Fc region, with the collagenous stalks pointing away from IgG as desired.[44] The details of the proposed interaction are shown in Fig. 4 of the docked structure.[44] The 19 C1q and 12 Fc contact residues identified in Table 2 from that study were used to replicate this predicted docked structure (Fig. 8e). The displacement of the Fab regions in our solution structure for intact rabbit IgG away from the Fc–C1q contact region permitted the C1q interactions with the top of the Fc region.

Stability of rabbit IgG

Antibodies represent a $30 billion industry and the detailed study of the solution properties of antibodies is necessary to maximize their potential as therapeutics.[2] Antibody behavior during manufacture, shipping and storage is important to understand, given that alterations may lead to undesired immunogenic effects.[45,46] This study has investigated not only rabbit IgG but also the fact that it is polyclonal. There are many applications and examples of using (cheaper) polyclonal antibodies for diagnostics and therapy. In these contexts, the unchanged rabbit IgG solution structures in different buffers and protein concentrations indicate that no internal structural

rearrangement of the Fab and Fc regions occurred within rabbit IgG. Thus, the $s_{20,w}$ values of the monomer and dimer were unchanged in a range of buffers. The two peaks *M1* and *M2* in the X-ray and neutron $P(r)$ curves were likewise unchanged in different buffers.

The increases in the percentage of dimer seen from the $c(s)$ and R_G analyses are attributable to the buffer in use. As high as 25% dimer formation was observed at low temperatures and in heavy water (Figs. 1e and 3e and f). Given that dimer may not be seen for monoclonal antibodies such as human IgG4,[8] dimer formation may result from specific sequences on the surface of the rabbit Fab region that promotes weak dimers with apparent K_D values between 70 and 350 μM. If dimers are formed by bivalent contacts at each of the two Fab regions in rabbit IgG (Fig. 7c), dimer formation will be cooperative. The weak interactions leading to dimer formation will be promoted by lower temperatures, as observed, as these will favor longer lifetimes for the interaction. The increased dimer formation in heavy water is attributable to the weaker solvation of the hydration shell surrounding the antibody. In distinction, the change of salt between 137 mM and 250 mM NaCl has a smaller effect on dimer formation.

Materials and Methods

Purification and composition of rabbit IgG

Polyclonal rabbit IgG (species *Oryctolagus cuniculus*) was generously supplied by Dr. Michael Brownleader (Generon, Maidenhead, Berkshire, UK). This was purified by gel filtration using a Superose 6 10/300 column (GE Healthcare), then concentrated using Amicon Ultra spin concentrator (50-kDa molecular mass cutoff) and dialyzed at 4 °C against the appropriate ultracentrifugation and scattering buffer (see below). Its sequence was taken from two crystal structures for rabbit Fc (PDB code 2VUO)[15] and rabbit Fab (PDB code 3NL4).[47] The 2VUO file included the C_H2 and C_H3 domains, and the 3NL4 file included the C_H1 and V_H domains and also a κ light chain with the C_L and V_L domains (GenBank code 340780374) (Supplementary Fig. S1). The hinge residues between the C_H1 and C_H2 domains were identified from CLUSTALW sequence alignments of the C_H1, C_H2 and C_H3 domains with the complete rabbit heavy-chain sequence (PDB code 3NL4; GenBank code AAA64252.1).[28] The N-linked oligosaccharides at Asn297 on the C_H2 domains (Supplementary Fig. S1) were taken to have a typical complex-type biantennary oligosaccharide structure with a $Man_3GlcNAc_2$ core and two NeuNAc.Gal.GlcNAc antennae.[48] In addition, rabbit IgG is 40% glycosylated by an O-linked oligosaccharide (assumed to be a NeuNAc.Gal.GalNAc trisaccharide) at a single Thr228 residue at an asymmetric hinge glycosylation site between the C_H1 and C_H2 domains.[34] A fourth N-linked oligosaccharide is located in about 15% of the Fab regions and was not considered further in this study.[34] The rabbit IgG molecular mass was calculated to be 143.9 kDa, its unhydrated volume was 185.6 nm^3, its hydrated volume was 244.3 nm^3 (based on a hydration of 0.3 g of water per gram of glycoprotein and an electrostricted volume of 0.0245 nm^3 per bound water molecule), its partial specific volume v was 0.731 ml/g and its absorption coefficient at 280 nm was 14.7 (1%, 1 cm pathlength).[18]

All data were recorded in phosphate-buffered saline with different NaCl concentrations. The standard buffer has a composition of 137 mM NaCl, 8.1 mM Na_2HPO_4, 2.7 mM KCl and 1.5 mM KH_2PO_4 (pH 7.4) and was termed PBS-137. When 137 mM NaCl was replaced by 50 mM NaCl or 250 mM NaCl, this was termed PBS-50 or PBS-250, respectively. The buffer densities were measured using an Anton Paar DMA 5000 density meter. The experimental values were used for data analyses and were compared with the theoretical values calculated by SEDNTERP.[49] This resulted in densities of 1.00540 g/ml for PBS-137 at 20 °C (theoretical, 1.00534 g/ml), 1.00174 g/ml for PBS-50 at 20 °C (theoretical, 1.00175 g/ml), 1.01030 g/ml for PBS-250 at 20 °C (theoretical, 1.00998 g/ml), 1.00752 g/ml for PBS-137 at 5 °C, 1.00270 g/ml for PBS-137 at 30 °C and 1.112381 g/ml for PBS-137 at 20 °C in 100% ^2H_2O.

Sedimentation velocity data for rabbit IgG

Analytical ultracentrifugation data for rabbit IgG were obtained on two Beckman XL-I instruments equipped with AnTi50 rotors. Sedimentation velocity data were acquired for rabbit IgG samples in PBS-50, PBS-137 and PBS-250 at 20 °C and also in PBS-137 at 5 °C and 30 °C and in PBS-137 with 100% ^2H_2O. Data were collected at rotor speeds of 40,000 r.p.m. and 50,000 r.p.m. in two-sector cells with column heights of 12 mm. Sedimentation analysis was performed using direct boundary Lamm fits of up to 500 scans using SEDFIT (version 12.1).[50,51] SEDFIT resulted in size-distribution analyses $c(s)$ that assume all species to have the same frictional ratio f/f_0. The final SEDFIT analyses used a fixed resolution of 200 and optimized the $c(s)$ fit by floating f/f_0 and the baseline until the overall root-mean-square deviations and visual appearance of the fits were satisfactory. The percentage of oligomers in the total loading concentration was derived using the $c(s)$ integration function.

X-ray and neutron scattering data for rabbit IgG

X-ray scattering data were obtained during a beam session in 16-bunch mode on Instrument ID02 at the European Synchrotron Radiation Facility, Grenoble, France, operating with a ring energy of 6.0 GeV on the Beamline ID02.[52] Storage ring currents ranged from 32 mA to 43 mA. Data were acquired using a fiber-optically coupled high sensitivity and dynamic range charge-coupled device detector (FreLoN) with a resolution of 512×512 pixels. A sample-to-detector distance of 3.0 m was used. Rabbit IgG at 20 °C only in PBS-137 and PBS-250 was studied at 10 concentrations between 0.5 mg/ml (3.5 μM) and 5.0 mg/ml (35 μM), in which samples of volume 100 μl were measured in a polycarboxylate capillary (diameter, 2 mm) that avoids protein deposits during exposures, with the sample being moved

continuously during beam exposure to reduce radiation damage. Sets of 10 time frames, with frames of duration 0.1 s or 0.2 s each, were acquired in quadruplicate as a control of reproducibility. Online checks during data acquisition confirmed the absence of radiation damage, after which the 10 frames were averaged. An initial X-ray beam session utilized rabbit IgG at 0.5 mg/ml (3.5 μM) to 5.0 mg/ml (35 μM) in PBS-137, which was measured in a quartz capillary (diameter, 1.75 mm).

Neutron scattering data were obtained on Instrument SANS2D at the pulsed neutron source ISIS at the Rutherford Appleton Laboratory, Didcot, UK.[53] A pulsed neutron beam was derived from proton beam currents of approximately 40 μA. SANS2D data were recorded with 4 m of collimation, a 4-m sample-to-detector distance, a 12-mm beam diameter and a wavelength range from 0.175 to 1.65 nm available by time of flight. Rabbit IgG samples were measured in 2-mm-thick rectangular quartz Hellma cells positioned in a thermostated rack at 20 °C and also at 6 °C and 37 °C. Data acquisitions lasted 1.5–3.5 h for four rabbit IgG samples at concentrations between 2.0 mg/ml (14 μM) and 7.0 mg/ml (49 μM) in PBS-137 prepared in heavy water.

In a given solute–solvent contrast, the radius of gyration R_G is a measure of structural elongation if the internal in homogeneity of scattering densities within the protein has no effect. Guinier analyses at low Q (where $Q=4\pi\sin\theta/\lambda$; 2θ is the scattering angle and λ is the wavelength) gives the R_G and the forward scattering at zero angle $I(0)$[54]:

$$\ln I(Q) = \ln I(0) - \frac{{R_G}^2 Q^2}{3}$$

This expression is valid in a $Q.R_G$ range up to 1.5. If the structure is elongated, the mean radius of gyration of cross-sectional structure R_{XS} and the mean cross-sectional intensity $[I(Q)Q]_{Q\to 10}$ is obtained from:

$$\ln[I(Q)Q] = [I(Q)Q]_{Q\to 0} - \frac{{R_{XS}}^2 Q^2}{2}$$

For immunoglobulins, the cross-sectional plot exhibits two regions, a steeper innermost one and a flatter outermost one,[55] and the two analyses are identified by $R_{XS\text{-}1}$ and $R_{XS\text{-}2}$, respectively. The R_G and R_{XS} analyses were performed using an interactive PERL script program SCTPL7 (J. T. Eaton and S. J. Perkins, unpublished software) on Silicon Graphics OCTANE Workstations. Indirect transformation of the scattering data $I(Q)$ in reciprocal space into real space to give the distance distribution function $P(r)$ was carried out using the program GNOM[56]:

$$P(r) = \frac{1}{2\pi^2}\int_0^\infty I(Q)Qr\sin(Qr)dQ$$

$P(r)$ corresponds to the distribution of distances r between volume elements. This yields the maximum dimension of the macromolecule L and its most commonly occurring distance vector M in real space. For this, the X-ray $I(Q)$ curve utilized up to 822 data points in the Q range between 0.09 nm^{-1} and 1.90 nm^{-1}. The neutron $I(Q)$ curve utilized up to 153 data points in the Q range between 0.07 nm^{-1} and 2.0 nm^{-1}.

Debye scattering and sedimentation coefficient modeling of rabbit IgG

A total of 5000 conformationally randomized rabbit IgG models were created by joining the rabbit Fab and Fc crystal structures (PDB codes 3NL4 and 2VUO, respectively) with conformationally randomized hinge peptides. Missing residues in the crystal structures were added using Discovery Studio v2.5 (Accelrys, San Diego, CA, USA). The hinge peptide was 224-CSKPTCPP-231. Starting from an extended β-strand conformation, we conformationally randomized the central six residues using molecular dynamics in the Discovery module of the molecular modeling software Insight II in order to create a library of 5000 conformations (Accelrys).[10] The length of the eight-residue peptide was constrained at the most extended length of 2.8 nm in order to avoid abnormally short hinge structures. The outermost residues were anchor points used to superimpose each hinge conformation onto the three Fab and Fc regions in order to create the full rabbit IgG model. Two different hinge conformations that were sampled at random were used to join the two Fab and Fc regions to create 5000 rabbit IgG models.

The X-ray or neutron scattering curve was calculated from each IgG model using sphere models for comparison with the experimental rabbit IgG curves. A cube-side length of 0.544 nm in combination with a cutoff of four atoms was used to convert the atomic coordinates into 1136 spheres that corresponded to the unhydrated structure. Because hydration shells are visible by X-rays, a hydration shell corresponding to 0.3 g of water per gram of protein was created using HYPRO,[57] giving an optimal total of 1470 hydrated spheres. The X-ray scattering curve $I(Q)$ was calculated using the Debye equation adapted to spheres.[58] Details are given elsewhere.[10,19] Steric overlap between the Fab and Fc regions was assessed using the number of spheres found in each model, where models showing less than 95% of the required total of 1470 spheres were discarded. Over 61% of the 5000 models showed no steric overlap. Next, the X-ray R_G, $R_{XS\text{-}1}$ and $R_{XS\text{-}2}$ values were calculated from the modeled curves in the same Q ranges used for the experimental Guinier fits. Models that passed R_G filters of ±5% of the experimental value were then ranked using a goodness-of-fit R-factor defined by analogy with protein crystallography and based on the experimental curves in the Q range extending to 1.9 nm^{-1}. For the neutron scattering modeling, the unhydrated sphere models were used to calculate the scattering curves. Over 72% of the 5000 models showed no steric overlap. The models created from neutron scattering were assessed as for the X-ray scattering models above. No correction was required for a flat incoherent background.

Sedimentation coefficients $s_{20,w}$ were calculated directly from the hydrated Debye sphere models using the program HYDRO.[59] They were also calculated from the atomic coordinates in the HYDROPRO shell modeling program using the default value of 0.31 nm for the atomic-element radius for all atoms to represent the hydration shell.[60] Previous applications of these calculations to antibodies are reviewed elsewhere.[24]

Artwork was prepared using PyMOL (DeLano Scientific†). Superimpositions of the Fc region were performed using

the align function within PyMOL. For the docking of the crystal structures for the Fc region and the C1q head, the web server algorithm PatchDock (version beta 1.3)‡ was used in order to take advantage of its ability to include specified residues as potential binding sites; the output was then refined using FIREDOCK from the same web site.[61]

PDB accession numbers

The 10 best-fit rabbit IgG models determined for each of the three buffers have been deposited in the PDB with the accession codes 4GDQ (PBS-137), 4GDR (PBS-250) and 4GDS (PBS-137 in heavy water).

Supplementary materials to this article can be found online at http://dx.doi.org/10.1016/j.jmb.2012.11.019

Acknowledgements

We thank Dr. Michael Brownleader (Generon) for generously providing rabbit IgG. We thank Dr. T. Narayanan at the European Synchrotron Radiation Facility in Grenoble and Dr. S. Rogers at ISIS for excellent instrumental support. This work was supported by the Biotechnology and Biological Sciences Research Council.

Received 5 August 2012;
Received in revised form 4 November 2012;
Accepted 15 November 2012
Available online 20 November 2012

Keywords:
analytical ultracentrifugation;
constrained modeling;
neutron scattering;
rabbit IgG;
X-ray scattering

† http://www.pymol.org/
‡ Available at http://bioinfo3d.cs.tau.ac.il/PatchDock/ and based on shape complementarity.

Abbreviations used:
FcR, Fc receptor; PDB, Protein Data Bank.

References

1. Hamilton, R. G. (2001). *The Human IgG Subclasses.* Calbiochem Corporation, La Jolla, CA.
2. Wang, X., Das, T. K., Singh, S. K. & Kumar, S. (2009). Potential aggregation prone regions in biotherapeutics: a survey of commercial monoclonal antibodies. *MAbs*, **1**, 254–267.
3. Brekke, O. H., Michaelson, T. E. & Sandlie, I. (1995). The structural requirements for complement activation by IgG: does it hinge on the hinge? *Immunol. Today*, **16**, 85–90.
4. Harris, L. J., Skaletsky, E. & McPherson, A. (1998). Crystallographic structure of an intact IgG1 monoclonal antibody. *J. Mol. Biol.* **275**, 861–872.
5. Saphire, E. O., Parren, P. W. H. I., Pantophlet, R., Zwick, M. B., Morris, G. M., Rudd, P. M. *et al.* (2001). Crystal structure of a neutralizing human IgG against HIV-1: a template for vaccine design. *Science*, **293**, 1155–1159.
6. Guddat, L. W., Herron, J. N. & Edmundson, A. B. (1993). Three-dimensional structure of a human immunoglobulin with a hinge deletion. *Proc. Natl Acad. Sci. USA*, **90**, 4271–4275.
7. Harris, L. J., Larson, S. B., Hassel, K. W., Day, J., Greenwood, A. & McPherson, A. (1992). The three-dimensional structure of an intact monoclonal antibody for canine lymphoma. *Nature*, **360**, 369–372.
8. Abe, Y., Gor, J., Bracewell, D. G., Perkins, S. J. & Dalby, P. A. (2010). Masking of the Fc region is human IgG4 by constrained X-ray scattering modeling: implications for antibody function and therapy. *Biochem. J.* **432**, 101–111.
9. Mayans, M. O., Coadwell, W. J., Beale, D., Symons, D. & Perkins, S. J. (1995). Demonstration by pulsed neutron scattering that the arrangement of the Fab and Fc fragments in the overall structures of bovine IgG1 and IgG2 in solution is similar. *Biochem. J.* **311**, 283–291.
10. Boehm, M. K., Woof, J. M., Kerr, M. A. & Perkins, S. J. (1999). The Fab and Fc fragments of IgA1 exhibit a different arrangement from that in IgG: a study by X-ray and neutron solution scattering and homology modeling. *J. Mol. Biol.* **286**, 1421–1447.
11. Furtado, P. B., Whitty, P. W., Robertson, A., Eaton, J. T., Almogren, A., Kerr, M. A. *et al.* (2004). Solution structure determination of monomeric human IgA2 by X-ray and neutron scattering, analytical ultracentrifugation and constrained modeling: a comparison with monomeric human IgA1. *J. Mol. Biol.* **338**, 921–941.
12. Sun, Z., Almogren, A., Furtado, P. B., Chowdhury, B., Kerr, M. A. & Perkins, S. J. (2005). Semi-extended solution structure of human myeloma immunoglobulin D determined by constrained X-ray scattering. *J. Mol. Biol.* **353**, 155–173.
13. Dangl, J. L., Wensel, T. G., Morrison, S. L., Stryer, L., Herzenberg, L. A. & Oi, V. T. (1988). Segmental flexibility and complement fixation of genetically engineered chimeric human, rabbit and mouse antibodies. *EMBO J.* **7**, 1989–1994.
14. Noelken, M. E., Nelson, C. A., Buckley, C. E., III & Tanford, C. (1965). Gross conformation of rabbit 7 S γ-immunoglobulin and its papain-cleaved fragments. *J. Biol. Chem.* **240**, 218–224.
15. Girardi, E., Holdom, M. D., Davies, A. D., Sutton, B. J. & Beavil, A. J. (2009). The crystal structure of rabbit IgG-Fc. *Biochem. J.* **417**, 77–83.
16. Perkins, S. J. & Bonner, A. (2008). Structure determinations of human and chimaeric antibodies by solution scattering and constrained molecular modelling. *Biochem. Soc. Trans.* **36**, 37–42.
17. Okemefuna, A. I., Nan, R., Gor, J. & Perkins, S. J. (2009). Electrostatic interactions contribute to the folded-back conformation of wild-type human factor H. *J. Mol. Biol.* **391**, 98–118.
18. Perkins, S. J. (1986). Protein volumes and hydration effects. *Eur. J. Biochem.* **157**, 169–180.

19. Perkins, S. J. (2001). X-ray and neutron scattering analyses of hydration shells: a molecular interpretation based on sequence predictions and modeling fits. *Biophys. Chem.* **93**, 129–139.
20. Gregory, L., Davies, K. G., Sheth, B., Boyd, J., Jefferis, R., Nave, C. & Burton, D. R. (1987). The solution conformations of the subclasses of human IgG deduced from sedimentation and small angle X-ray scattering studies. *Mol. Immunol.* **24**, 821–829.
21. Longman, E., Kreusel, K., Tendler, S. B., Fiebrig, I., King, K., Adair, J. *et al.* (2003). Estimating domain orientation of two human antibody IgG4 chimeras by crystallohydrodynamics. *Eur. Biophys. J.* **32**, 503–510.
22. Lu, Y., Harding, S. E., Michaelsen, T. E., Longman, E., Davis, K. G., Ortega, A. *et al.* (2007). Solution conformation of wild-type and mutant IgG3 and IgG4 immunoglobulins using crystallohydrodynamics: possible implications for complement activation. *Biophys. J.* **93**, 3733–3744.
23. Richardson, J. S. & Richardson, D. C. (1989). Principles and patterns of protein conformation. In *Prediction of Protein Structure and the Principles of Protein Conformation* (Fasman, G. D., ed.), pp. 1–98, Plenum Press, New York, NY.
24. Perkins, S. J., Okemefuna, A. I., Nan, R., Li, K. & Bonner, A. (2009). Constrained solution scattering modeling of human antibodies and complement proteins reveals novel biological insights. *J. R. Soc., Interface*, **6**, S679–S696.
25. Okemefuna, A. I., Stach, L., Rana, S. R., Buetas, A. J. Z., Gor, J. & Perkins, S. J. (2010). C-reactive protein exists in an NaCl concentration-dependent pentamer–decamer equilibrium in physiological buffer. *J. Biol. Chem.* **285**, 1041–1052.
26. Mage, R. G., Bernstein, K. E., McCartney-Francis, N., Alexander, C. B., Young-Cooper, G. O., Padlan, E. A. & Cohen, G. H. (1984). The structural and genetic basis for expression of normal and latent V_Ha allotypes of the rabbit. *Mol. Immunol.* **21**, 1067–1081.
27. Esteves, P. J., Lanning, D., Ferrand, N., Knight, K. L., Zhai, S. K. & van der Loo, W. (2004). Allelic variation at the *V_Ha* locus in natural populations of rabbit (*Oryctolagus cuniculus* L.). *J. Immunol.* **172**, 1044–1053.
28. Bernstein, K. E., Alexander, C. B. & Mage, R. G. (1983). Nucleotide sequence of a rabbit IgG heavy chain from the recombinant F-I haplotype. *Immunogenetics*, **18**, 387–397.
29. Emorine, L., Sogn, J. A., Trinh, D., Kindt, T. J. & Max, E. E. (1984). A genomic gene encoding the b5 rabbit immunoglobulin κ constant region: implications for latent allotype phenomenon. *Proc. Natl Acad. Sci. USA*, **81**, 1789–1793.
30. van der Loo, W., Mougel, F., Bouton, C., Sanchez, M. S. & Monnerot, M. (1999). The allotypic patchwork pattern of the rabbit *IGKC1* allele *b5wf*: genic exchange or common ancestry? *Immunogenetics*, **49**, 7–14.
31. Akimenko, M. A., Heidmann, O. & Rougeon, F. (1984). Complex allotypes of the rabbit immunoglobulin κ light chains are encoded by structural alleles. *Nucleic Acids Res.* **12**, 4691–4701.
32. Benammar, A. & Cazenave, P. A. (1982). A second rabbit κ isotype. *J. Exp. Med.* **156**, 585–595.
33. Popokov, M., Jendreyko, N., Gonzalez-Sapienza, G., Mage, R. G., Rader, C. & Barbas, C. F., III (2004). Human/mouse cross-reactive anti-VEGF receptor 2 recombinant antibodies selected from an immune b9 allotype rabbit antibody library. *J. Immunol. Methods*, **288**, 149–164.
34. Fanger, M. W. & Smyth, D. G. (1972). The oligosaccharide units of rabbit immunoglobulin G. *Biochem. J.* **127**, 757–765.
35. Langone, J. J., Boyle, M. D. P. & Borsos, T. (1977). ^{125}I protein A: applications to the quantitative determination of fluid phase and cell-bound IgG. *J. Immunol. Methods*, **18**, 281–293.
36. Ravetch, J. V. & Kinet, J.-P. (1991). Fc receptors. *Annu. Rev. Immunol.* **9**, 457–492.
37. Tamm, A. & Schmidt, R. E. (1997). IgG binding sites on human Fcγ receptors. *Int. Rev. Immunol.* **16**, 57–85.
38. Radaev, S. & Sun, P. (2001). Recognition of immunoglobulins by Fcγ receptors. *Mol. Immunol.* **38**, 1073–1083.
39. Daëron, M. (1997). Fc receptor biology. *Annu. Rev. Immunol.* **15**, 203–234.
40. Sondermann, P., Huber, R., Oosthuizen, V. & Jacob, U. (2000). The 3.2 Å crystal structure of the human IgG1 Fc fragment–FcγRIII complex. *Nature*, **406**, 267–273.
41. Krapp, S., Minura, Y., Jefferis, R., Huber, R. & Sondermann, P. (2003). Structural analysis of human IgG-Fc glycoforms reveals a correlation between glycosylation and structural integrity. *J. Mol. Biol.* **325**, 979–989.
42. Nimmerjahn, F. & Ravetch, J. V. (2008). Fcγ receptors as regulators of immune responses. *Nat. Rev., Immunol.* **8**, 34–47.
43. Radaev, S., Motykai, S., Fridman, W.-H., Sautes-Fridman, C. & Sun, P. D. (2001). The structure of a human type III Fcγ receptor in complex with Fc. *J. Biol. Chem.* **276**, 16469–16477.
44. Schneider, S. & Zacharias, W. (2012). Atomic resolution model of the antibody Fc interaction with the complement C1q component. *Mol. Immunol.* **51**, 66–72.
45. Cromwell, M. E. M., Hilario, E. & Jacobson, F. (2006). Protein aggregation and bioprocessing. *AAPS J.* **8**, E572–E579.
46. Sukumar, M., Doyle, B. L., Combs, J. L. & Pekar, A. H. (2004). Opalescent appearance of an IgG1 antibody at high concentrations and its relationship to noncovalent association. *Pharm. Res.* **21**, 1087–1093.
47. Luecke, H., Glabe, G. G. & Arai, H. (2010). Crystal structure of amyloid prefibrillar-oligomer-specific rabbit Fab. Protein Data Bank accession code 3NL4.
48. Raju, T. S., Briggs, J. B., Borge, S. M. & Jones, A. J. (2000). Species-specific variation in glycosylation of IgG: evidence for the species-specific sialylation and branch-specific galactosylation and importance for engineering recombinant glycoprotein therapeutics. *Glycobiology*, **10**, 477–486.
49. Laue, T. M., Shah, B. D., Ridgeway, T. M. & Pelletier, S. L. (1992). Computer-aided interpretation of analytical sedimentation data for proteins. In *Analytical Ultracentrifugation in Biochemistry and*

Polymer Science (Harding, S. E., Rowe, A. J. & Horton, J. C., eds), pp. 90–125, The Royal Society of Chemistry, Cambridge, U.K.
50. Schuck, P. (1998). Sedimentation analysis of non-interacting and self-associating solutes using numerical solutions to the Lamm equation. *Biophys. J.* **75**, 1503–1512.
51. Schuck, P. (2000). Size-distribution analysis of macromolecules by sedimentation velocity ultracentrifugation and lamm equation modeling. *Biophys. J.* **78**, 1606–1619.
52. Narayanan, T., Diat, O. & Bosecke, P. (2001). SAXS and USAXS on the high brilliance beamline at the ESRF. *Nucl. Instrum. Methods Phys. Res., Sect. A*, **467–468**, 1005–1009.
53. Heenan, R. K., Rogers, S. E., Turner, D., Terry, A. E., Treadgold, J. & King, S. M. (2011). Small angle neutron scattering using Sans2d. *Neutron News*, **22**, 19–21.
54. Glatter, O. & Kratky, O. (1982). *Small Angle X-ray Scattering.* Academic Press, New York, NY.
55. Pilz, I., Kratky, O., Licht, A. & Sela, M. (1973). Shape and volume of anti-poly(D-alanyl) antibodies in the presence and absence of tetra-D-alanine as followed by small-angle X-ray scattering. *Biochemistry*, **12**, 4998–5005.
56. Semenyuk, A. V. & Svergun, D. I. (1991). GNOM—a program package for small-angle scattering data-processing. *J. Appl. Crystallogr.* **24**, 537–540.
57. Ashton, A. W., Boehm, M. K., Gallimore, J. R., Pepys, M. B. & Perkins, S. J. (1997). Pentameric and decameric structures in solution of the serum amyloid P component by X-ray and neutron scattering and molecular modeling analyses. *J. Mol. Biol.* **272**, 408–422.
58. Perkins, S. J. & Weiss, H. (1983). Low resolution structural studies of mitochondrial ubiquinol:cytochrome *c* reductase in detergent solutions by neutron scattering. *J. Mol. Biol.* **168**, 847–866.
59. Garcia de la Torre, J., Navarro, S., Martinez, M. C. L., Diaz, F. G. & Cascales, J. L. (1994). HYDRO: a computer program for the prediction of hydrodynamic properties of macromolecules. *Biophys. J.* **67**, 530–531.
60. GarciadelaTorre, J., Huertas, M. L. & Carrasco, B. (2000). Calculation of hydrodynamic properties of globular proteins from their atomic-level structure. *Biophys. J.* **78**, 719–730.
61. Schneidman-Duhovny, D., Inbar, Y., Nussinov, R. & Wolfson, H. J. (2005). PatchDock and SymmDock: servers for rigid and symmetric docking. *Nucleic Acids Res.* **33**, W363–W367.